Journal of Colloid and Interface Science 354 (2011) 630–636

Contents lists available at ScienceDirect

Journal of Colloid and Interface Science

www.elsevier.com/locate/jcis

BiOBr hierarchical microspheres: Microwave-assisted solvothermal synthesis, strong adsorption and excellent photocatalytic properties

Lei Zhang [a], Xiao-Feng Cao [a], Xue-Tai Chen [a,*], Zi-Ling Xue [b]

[a] State Key Laboratory of Coordination Chemistry, Nanjing National Laboratory of Microstructures, School of Chemistry and Chemical Engineering, Nanjing University, Nanjing 210093, PR China
[b] Department of Chemistry, The University of Tennessee, Knoxville, TN 37996-1600, USA

ARTICLE INFO

Article history:
Received 5 October 2010
Accepted 15 November 2010
Available online 20 November 2010

Keywords:
Microstructure
Mesocrystal
Photocatalytic

ABSTRACT

Two kinds of BiOBr nanosheets-assembled microspheres were successfully prepared via a facile, rapid and reliable microwave-assisted solvothermal route, employing $Bi(NO_3)_3{\cdot}5H_2O$ and cetyltrimethylammonium bromide (CTAB) as starting reagents in the absence or presence of oleic acid. The phase and morphology of the products were characterized by powder X-ray diffraction (XRD), energy dispersive spectrometry (EDS), selected area electron diffraction (SAED), high resolution transmission electron microscopy (HRTEM) and scanning electron microscopy (SEM). Experiments indicated that the formation of these building blocks of microspheres could be ascribed to the self-assembly of nanoparticles according to mesocrystal growth mode. Interestingly, both samples exhibited not only strong adsorption abilities, but also excellent photocatalytic activities for methyl orange (MO), rhodamine B (RhB) and phenol. The resulting BiOBr hierarchical microspheres are very promising adsorbents and photocatalysts for the treatment of organic pollutants.

1. Introduction

Effluents from the textile industries are important sources of water pollution, because dyes in wastewater undergoes chemical as well as biological changes, consume dissolved oxygen, destroy aquatic life and endanger human health. Therefore, it is necessary to treat textile effluents prior to their discharge into the receiving water [1–6]. Up to now, physical adsorption and photocatalytic degradation are considered as two effective and convenient methods for removing of organic dyes [7–12]. With the intensive development of materials research, various micro- and nano-materials have already been adopted for the treatment of environmental pollutants due to their excellent photocatalytic activities or strong adsorption capacities, such as Zn_2GeO_4, ZnO, TiO_2, silver titanates nanobelts and magnesium silicate hollow spheres [13–19]. As well known, one of the ultimate goals of nanotechnology for the pollutant treatment from wastewater is to develop ideal materials with low cost and strong mechanical structures as well as high removal capacities and fast photocatalytic degradation rates for dyes [20,21]. Materials with hierarchical nano/microstructures meet these criteria well. Their novel structures lead to large BET surface area and more efficient transport for the reactant molecules, which contribute to high adsorption capacities and fast degradation rates.

Bismuth oxyhalides, BiOX (X = Cl, Br, I), are of great importance because of their optical properties and applications as catalysts, ferroelectric materials, and pigments [22–25]. They can also be used as excellent photocatalysts to decompose organic compounds for purifying textile dye from polluted wastewater. Recently, hierarchical structured BiOBr microspheres have attracted much attention and have already been successfully prepared via various synthetic routes. For example, Tang's group demonstrated the ethylene glycol-assisted solvothermal synthesis of three-dimensional (3-D) microspherical BiOBr architectures assembled by nanosheets [26]. Zhang and coworkers developed a general one-pot solvothermal process to prepare hierarchical BiOX (X = Cl, Br, I) microspheres by employing ethylene glycol as solvent [27]. However, to the best of our knowledge, it is still rare in the literature about the preparation of BiOBr hierarchical microspheres based on the self-assembly of mesocrystal nanosheets through a microwave-assisted solvothermal route. In recent years, the microwave heating has been widely applied in chemical reactions and materials synthesis with several advantages: (1) shorter reaction time; (2) more uniform product dimensions and composition; (3) easiness to tune compositions of the products [28–31].

Herein, we report the successful synthesis of BiOBr hierarchical microspheres constructed by mesocrystal nanosheets through a facile and rapid microwave-assisted solvothermal route. Furthermore, the adsorption abilities and photocatalytic properties of BiOBr samples were studied. Compared with those reported in

* Corresponding author. Fax: +86 25 83314502.
E-mail address: xtchen@netra.nju.edu.cn (X.-T. Chen).

0021-9797/$ - see front matter © 2010 Elsevier Inc. All rights reserved.
doi:10.1016/j.jcis.2010.11.042

the literatures, our work presents some distinct differences. First, two kinds of novel BiOBr hierarchical microspheres are obtained. Second, both products possess excellent adsorption and photocatalytic abilities. Third, the use of microwave heating makes the reaction time much shorter than conventional heating mode and affords a facile and rapid preparation pathway to novel BiOBr nanoarchitectures.

2. Materials and methods

2.1. Synthesis

All the reagents were purchased from Shanghai Chemical Company and used without further purification. All the samples were prepared in a microwave system (2.45 GHz, 200 W, Discover S-Class, CEM) equipped with in situ magnetic stirring, in which the exposure time and temperature were programmed. The automatic temperature-control system allowed continuous monitoring and control (1 °C) of the internal temperature of reaction systems. The preset profile (desired time and temperature) was followed automatically by continuously adjusting the applied microwave power. In the preparation procedure of sample **1** (**S1**), $Bi(NO_3)_3 \cdot 5H_2O$ (0.4851 g) and CTAB (Br source, 0.5 g) were dissolved in 15 mL of diethylene glycol (DEG) to form a homogeneous solution. Then, the solution was transferred into a 35 mL round-bottom flask. After treating the mixture at 180 °C for 10 min under microwave irradiation, it was cooled to room temperature rapidly by air compressor. The product was collected, washed with deionized water and absolute ethanol, and dried in a vacuum at 60 °C for 6 h. For the preparation of sample **2** (**S2**), 5 mL of DEG was replaced by oleic acid with the same volume, keeping other experimental conditions constant. The reaction parameters of the BiOBr samples are listed in Table 1.

2.2. Characterization

The products were characterized by X-ray powder diffraction (XRD) with a Shimadzu XRD-6000 powder X-ray diffractometer with Cu Kα radiation (λ = 1.5418 Å), recorded with 2θ ranging from 10° to 70°. SAED and HRTEM were carried out on a JEM-2100 high resolution transmission microscope, employing an accelerating voltage of 200 kV. SEM images and EDS of the products were obtained on field emission scanning electron microanalyser (Hitachi S-4800), employing the accelerating voltage of 5 or 20 kV. The UV–vis diffusion reflectance spectrum (DRS) of the sample was analyzed with a UV–vis spectrophotometer (UV-3600, Shimadzu, Japan). The Brunauer–Emmett–Teller (BET) surface area was measured using a Micrometrics ASAP 2010.

2.3. Adsorption measurement of RhB (pH = 4) and MO (pH = 6)

All the adsorption experiments were carried out in dark. 0.02 g of adsorbent (**S1** and **S2**) were introduced to different initial concentration of RhB or MO solutions (20 mL) in the dark. At given irradiated intervals, approximately 3 mL of the reaction suspension was sampled, and separated by a centrifugal machine. The adsorption spectrum of the filtrate was measured on a UV–vis spectrophotometer (UV-3600, Shimadzu, Japan).

2.4. Photocatalytic activities measurement of MO, RhB and phenol aqueous solution

The photocatalytic degradation of RhB, MO or phenol aqueous solution was conducted in an XPA-photochemical reactor (Xujiang Electromech-anical Plant, Nanjing, China) equipped with a 500 W high-pressure mercury lamp. An electric fan and cycled condensate water were used to prevent thermal catalytic effects. 0.02 g of BiOBr photocatalyst was introduced into each of a series of Pyrex reactors containing 20 mL of dyes solution (60 mg/L) or phenol aqueous solution (20 mg/L) at room temperature under air, respectively. Before light was turned on, the solution was continuously stirred for 40 min in the dark to ensure the establishment of an adsorption–desorption equilibrium. During irradiation, ~5 mL of the suspension was continually taken from the reactor at given time intervals. The photocatalyst powders and the pollutions solution were separated by a centrifugal machine. The MO, RhB and phenol concentration was analyzed through a UV–vis spectrophotometer (UV-3600, Shimadzu, Japan).

3. Results and discussion

The phase and crystallographic structure of the as-obtained samples were examined by XRD and EDS. Fig. 1 depicts the XRD patterns of the BiOBr hierarchical microspheres prepared under various conditions (**S1** and **S2**). It can be found that the XRD patterns of these two samples present similar profiles. All the reflection peaks could be indexed to a pure tetragonal phase BiOBr, which are in good agreement with the literature values (JCPDS file Card No. 73-2061). The wide peaks imply small crystalline size of the products. No other impurity peak is detected. Additional evidence of the formation of BiOBr came from energy dispersion X-ray analysis. Fig. 2 shows the energy dispersion X-ray spectrum (EDS) of the as-prepared products. The peaks of Bi, Br and O can be easily found. The C peak in the spectrum can be attributed to CTAB molecule adsorbed by the sample.

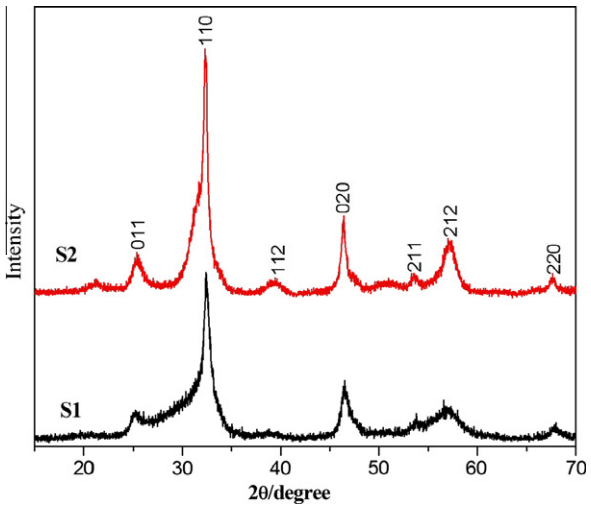

Fig. 1. XRD patterns of BiOBr hierarchical microspheres prepared under various conditions (**S1** and **S2**).

Table 1
The main reaction parameters and results of the control experiments performed at 180 °C for 10 min.

No	Amount of $Bi(NO_3)_3 \cdot 5H_2O$ (mol)	Amount of CTAB (g)	Reaction medium	Morphology and Size	BET surface area (m^2/g)
S1	0.001	0.5	15 mL DEG	Hierarchical spheres (3–5 μm)	35.4
S2	0.001	0.5	10 mL DEG + 5 mL oleic acid	Hierarchical spheres (4 μm)	7.3

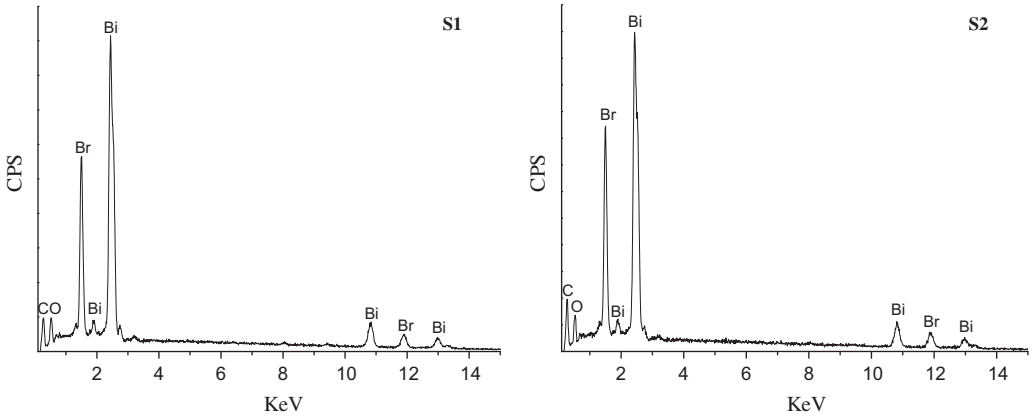

Fig. 2. EDS spectra of BiOBr hierarchical microspheres prepared under various conditions (**S1** and **S2**).

The microstructure and morphology of the product were investigated by SEM. As shown in Fig. 3a, one can find that **S1** is comprised of many microspheres with the range from 3 to 5 μm in diameters. A high magnification SEM image of an individual microsphere shows that the as-prepared product is constructed of many nanosheets (Fig. 3b). Careful observation reveals that there are great deal of nanopores in the surface of microspheres, which is formed by the stacking of these nanosheets. If 5 mL of oleic acid was introduced, keeping other experimental parameters constant, BiOBr nanosheets-assembled microspheres with relatively good dispersion and uniform diameters of ~4 μm were obtained (**S2**, Fig. 3c and d). It should be noted that the presence of oleic acid did not change the morphology of these building blocks. However, it could have important influence on the stacking mode of constructing units and resulted in the different pore structure in the surface of microspheres compared with **S1**.

The typical SAED pattern and HRTEM images taken from the selected area of nanosheets, which dropped from the integrated microspheres (**S1** and **S2**), were shown in Fig. 4. TEM observations clearly reveal that these nanosheets are constructed by much smaller particles (Fig. 4a and d), which can well explain the broadening of XRD peaks. The rough surfaces of the nanosheets suggest a different crystallization mechanism from the classical ion-by-ion growth. As well known, there are generally two pathways with regard to the crystallization process. The first one is so-called classical crystallization in which the crystal grows on the stable nuclei via ion-by-ion addition and unit replication. The second one is nonclassical crystallization including oriented attachment and mesocrystallization [32–37]. Oriented attachment is described as the spontaneous assembly of adjacent particles sharing a common crystallographic orientation by crystallographic fusion at the planar interface. If the nanoparticles are coated by some organic components, they can form a mesocrystal via mesoscale assembly, possibly followed by fusion to an isooriented crystal and finally to a single crystal [38–41]. Based on the above experimental results, we consider that the formation of nanosheets can be ascribed to mesocrystal growth. Actually, this point can be confirmed by the results of SAED and HRTEM images. The appearance of periodic diffraction spots (Fig. 4c and f) indicates that all of the small nanoparticles in the selected area have self-assembled into highly oriented

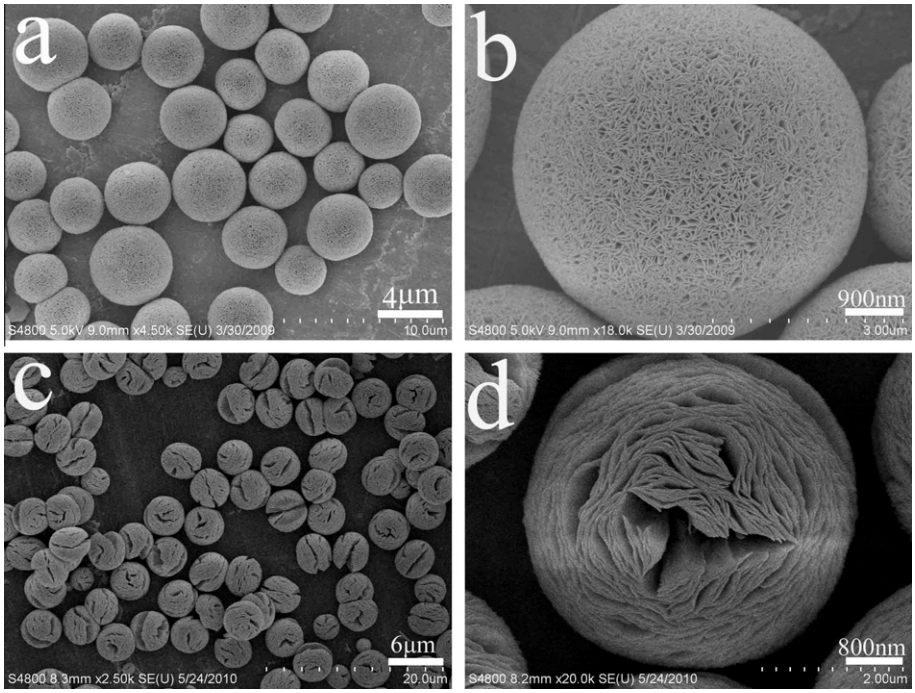

Fig. 3. SEM images of BiOBr hierarchical microspheres prepared under various conditions: (a and b) **S1** and (c and d) **S2**.

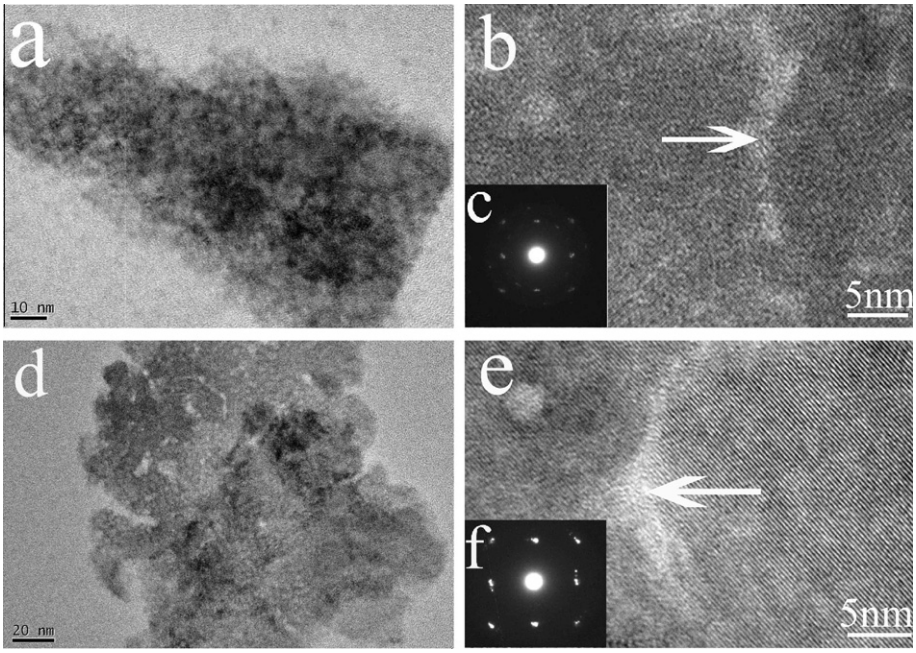

Fig. 4. TEM, HRTEM images and SAED patterns of BiOBr hierarchical microspheres prepared under various conditions: (a–c) **S1** and (d–f) **S2**.

aggregates and diffract as a single crystal. The SAED pattern shows that some diffraction spots have been elongated slightly, implying that small misorientations deviating from perfect alignment [42,43]. The existence of mesopores (marked by arrow in Fig. 4b and e) during the assembly characteristic of the mesocrystal is also observed in the HRTEM image, which further confirm that the formation of nanosheets originates from the self-assembly of small nanoparticles according to the mesocrystal growth mode. These produced mesocrystal nanosheets can further self-assemble to BiOBr hierarchical microspheres under microwave treatment.

Originally, these two kinds of hierarchical microspheres were used to decompose the MO and RhB dye solution (15 mg/L). However, unexpected results were observed. As shown in Fig. 5, one can find that both samples exhibit excellent adsorption capacity and **S1** owes the stronger adsorption ability. Within 40 min, about 93% of MO solution can be adsorbed by **S1**. When **S2** is employed as adsorbent, this value is 22%. This phenomenon has not been reported in previous literatures related to BiOBr, which may be attributed to their novel structures and large BET surface areas (Table 1). Compared with **S1**, the BET surface area of **S2** is much small, which can be ascribed to the existence of oleic acid. As mentioned above, the addition of oleic acid has important influence on the stacking mode of constructing units and results in the different pore structure in the surface of microspheres. In addition, some oleic acid rests on the surface of **S2** may be also responsible for the reduction of BET surface area. Adsorption isotherms of MO with different initial concentrations for 40 min of adsorption are illustrated in Fig. 6a (**S1**). It is clear that the adsorption amount increases first with increasing of initial concentration of MO solution and then reaches a saturation value. The Langmuir adsorption model is used to represent the relationship between the amount of dye adsorbed at equilibrium (q_e, mg/g) and the equilibrium solution concentration (C_e, mg/L, Eqs. (1) and (2) [44]:

$$q_e = q_m b C_e/(1 + bC_e) \tag{1}$$

$$C_e/q_e = C_e/q_m + 1/q_m b \tag{2}$$

where q_m (mg/g) is the maximum adsorption capacity, corresponding to complete monolayer coverage, and b is the equilibrium constant. When such a model is employed to analyze the adsorption isotherms, the experimental data fit the Langmuir adsorption isotherm well. The maximum removal capacities (q_m) of **S1** is found to be 15.3 mg/g for MO (Fig. 6b).

Before the photocatalytic activity characterization, it is important to study the optical absorption of the as-prepared BiOBr microspheres because the UV–vis absorption edge is relevant to the bandgap of semiconductor catalyst. The diffuse reflectance data is used to calculate the absorption coefficient from the Kubelka–Munk (KM) function, defined as:

$$F(R_\infty) = \alpha/S = (1 - R_\infty)^2/R_\infty \tag{3}$$

Here α, S and $F(R_\infty)$ is the absorption coefficient, scattering coefficient and KM function, respectively. As a crystalline semiconductor, it is well known that the optical absorption near the band edge follows the formula:

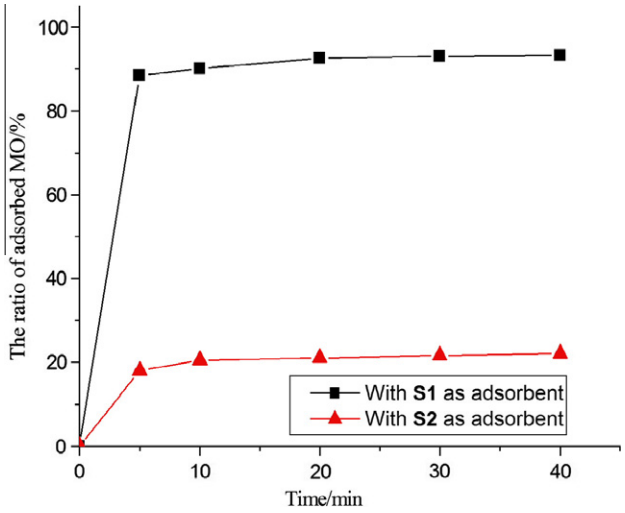

Fig. 5. Adsorption kinetics of MO removal with BiOBr hierarchical microspheres (**S1** and **S2**).

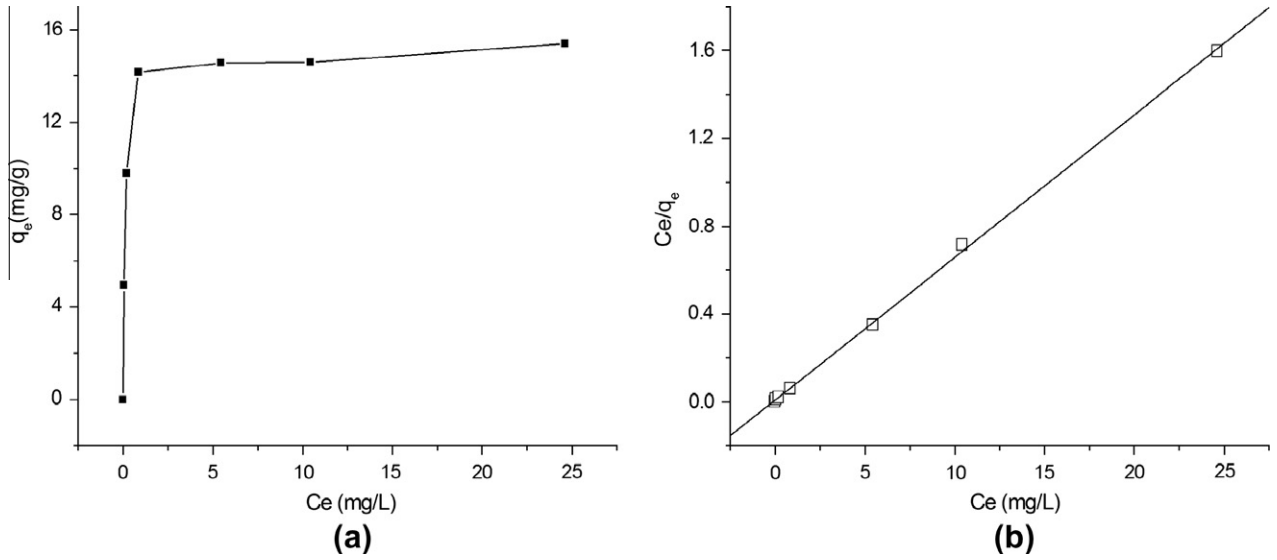

Fig. 6. Langmuir adsorption isotherm (a) and fitting langmuir adsorption isotherm (b) of MO for 40 min employing **S1** as adsorbent (pH = 6).

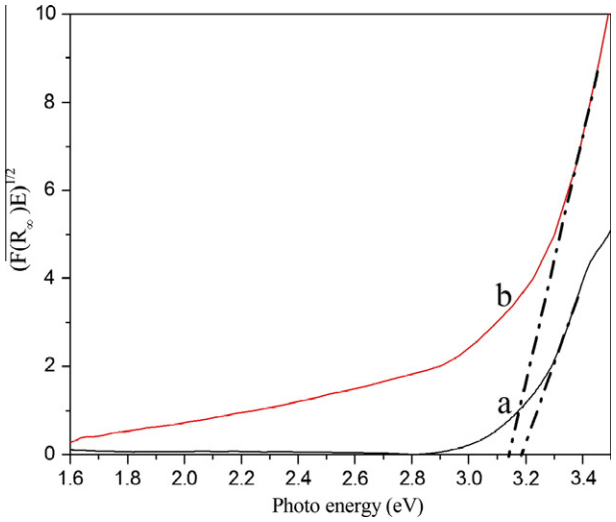

Fig. 7. Plots of $F(R_\infty)$ versus photo energy for the estimation of the optical absorption edge energy for **S1** (a) and **S2** (b).

$$\alpha E = C(E - E_g)^n \tag{4}$$

Here α, E, E_g and C is the absorption coefficient, incident photon energy, the optical absorption edge energy and a constant, respectively. The exponent n is dependent on the type of optical transition as a result of photon absorption. The exponent n is assigned a value of 1/2, 3/2, 2, and 3 for direct allowed, direct forbidden, indirect allowed, and indirect forbidden transition, respectively. For the diffused reflectance spectra, the KM function can be used instead of α for estimation of the optical absorption edge energy [45–47]. In order to determine E_g, we have measured the diffuse reflectance spectra of the **S1** and **S2** samples (Fig. 7). The intercept of the line on abscissa $[F(R_\infty)E = 0]$ give the values of optical absorption edge energy to be 3.17 and 3.14 eV for **S1** and **S2**, respectively. Taking into account the novel 3-D architectures with nanoscale building blocks, micrometer size, as well as UV light bandgap, the as-obtained BiOBr 3-D architectures should have excellent photocatalytic activities under UV irradiation.

To demonstrate the potential application of these two kinds of hierarchical microspheres in the degradation of organic contami-

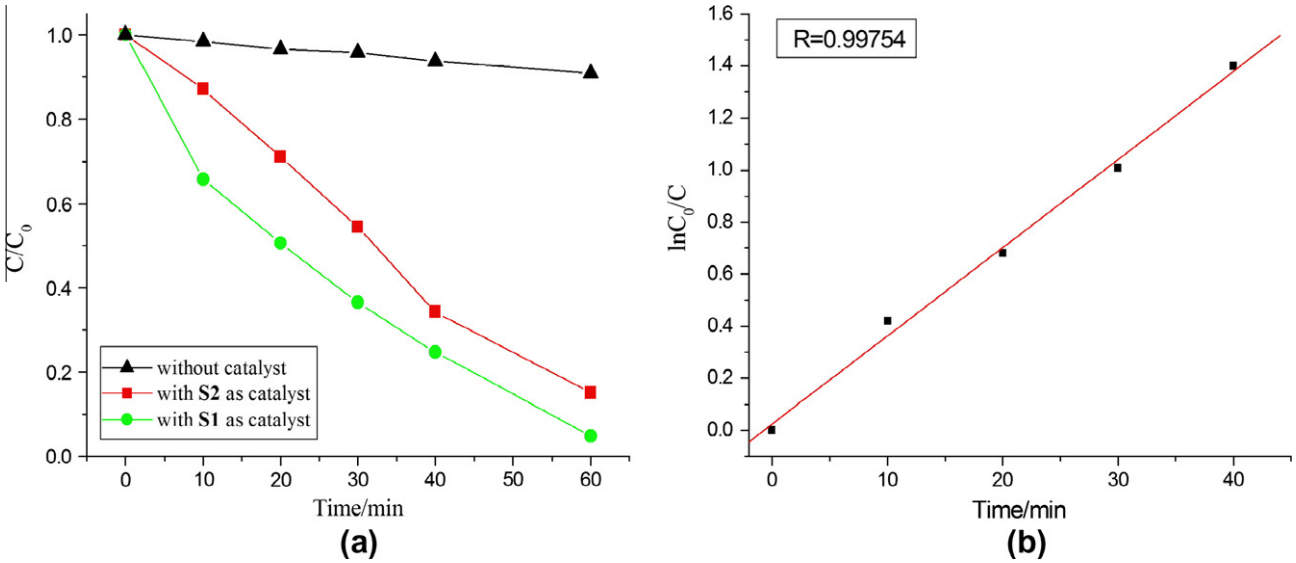

Fig. 8. (a) Photodegradation efficiencies of MO as a function of irradiation time and (b) kinetics of MO decolorization in solutions (**S1**).

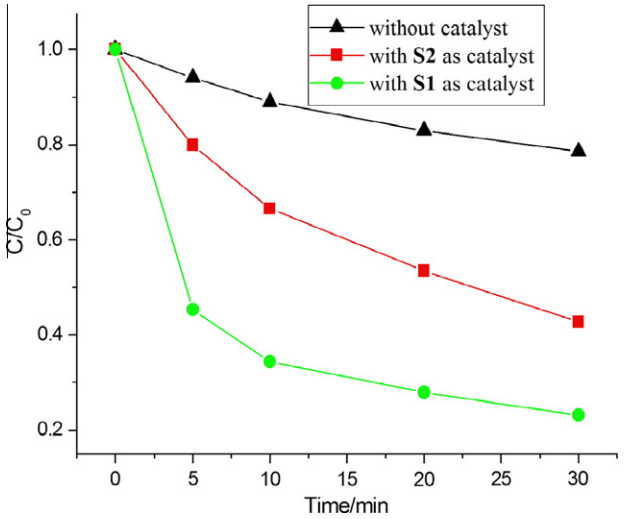

Fig. 9. Photodegradation efficiencies of RhB as a function of irradiation time.

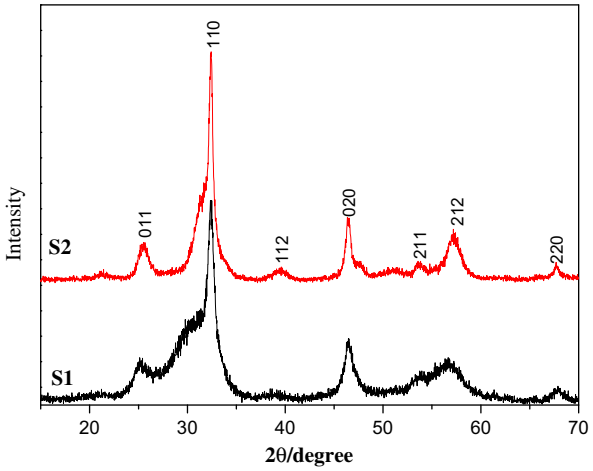

Fig. 11. XRD patterns of **S1** and **S2** after photocatalytic reaction.

nants, we investigated their photocatalytic activities by choosing the photocatalytic degradation of MO or RhB with high concentrations as a model reaction, which is much higher than the reported values related to BiOBr [26,27]. Fig. 8 shows the photocatalytic degradation of MO on **S1** and **S2**, presenting the concentration changes of MO at 464 nm as a function of irradiation time during the degradation process. It is known that the dye can undergo self-photolysis under UV irradiation. In our experiments, only 9% of MO is photolyzed after 60 min reaction in the absence of photocatalyst. In contrast, almost 96% of MO has been photolyzed employing **S1** as photocatalyst in the same irradiation time. When **S2** is used, this decomposition percentage is 85%. These experimental results indicate that both products can greatly degrade MO and **S1** owes the better degradation ability. To detailed analysis the photocatalysis kinetics of the MO degradation in our experiments, we apply the pseudo-first order model as expressed by Eq. (5), which is generally used for photocatalytic degradation process if the initial concentration of pollutant is low [48,49].

$$\ln(C_0/C) = kt \tag{5}$$

The C_0 and C are the concentrations of organic dye in solution at time 0 and t, respectively, and k is the pseudo-first-order rate constant. Fig. 8b is the photocatalytic reaction kinetics of MO degradation in solution on the basis of the data plotted in Fig. 8a employing **S1** as catalyst. As can be seen, a rather good correlation to the pseudo-first-order reaction kinetics ($R > 0.99$) is found. When RhB is used as a model pollutant, the two products also exhibit excellent photocatalytic activities for degradation of RhB under UV light irradiation (Fig. 9). In order to understand that the degradation abilities of the products can be ascribed to direct or indirect photocatalysis, phenol in aqueous solution under UV light irradiation was also studied. Fig. 10 displays the changes of the phenol concentration versus the reaction time over **S1** and **S2**, which clearly indicate that with identical UV light exposure, both samples show high photocatalytic activities and **S1** owes the better degradation ability. The decomposition percentage for **S1** and **S2** is 99% and 94%, respectively. Additionally, the XRD patterns of **S1** and **S2** after the photocatalytic reaction in Fig. 11 reveal that the phase and structure remain intact. SEM observations also show little change in the morphology (Fig. 12). These results indicate that the 3-D BiOBr microspheres prepared by this method are stable for the photocatalysis of pollutant molecules, which is important for its application.

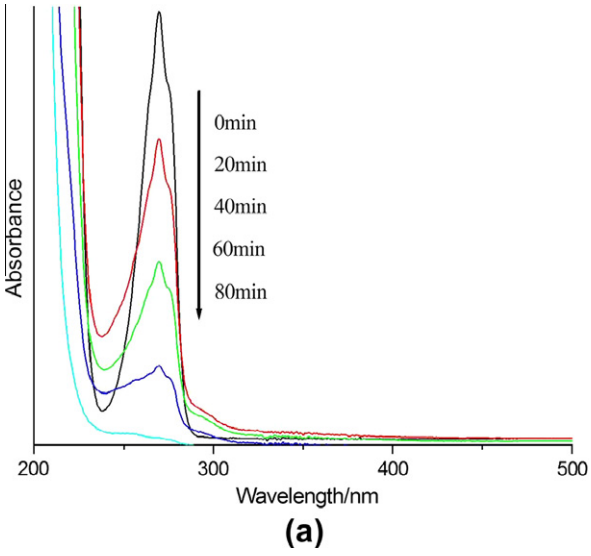

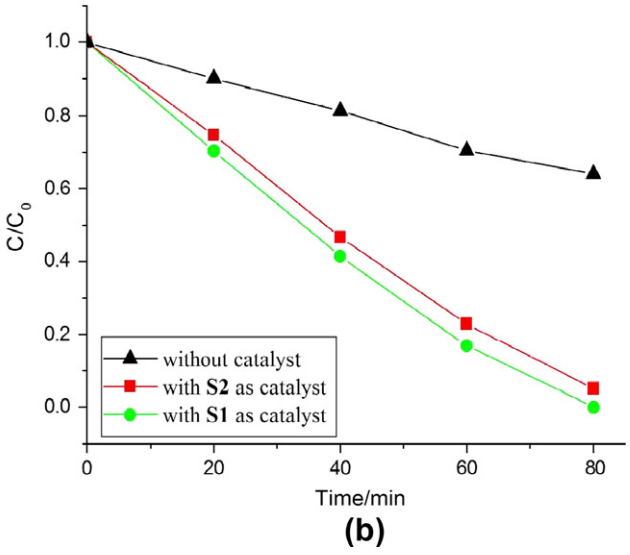

Fig. 10. (a) Absorption spectra of the phenol solution in the presence of **S1** under exposure to UV light and (b) photodegradation efficiencies of phenol as a function of irradiation time (**S1** and **S2**).

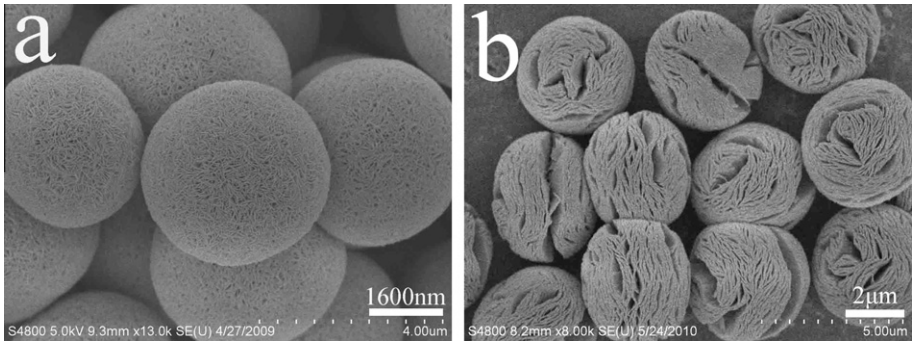

Fig. 12. SEM images of **S1** (a) and **S2** (b) after photocatalytic reaction.

Several reasons may account for the high photocatalytic activity of **S1** and **S2**. First, it is generally accepted that the catalytic process is mainly related to the adsorption and desorption of molecules on the surface of the catalyst. The high BET surface areas lead to more unsaturated surface coordination sites exposed to the pollution molecules in solution. These novel microspheres possess unusual hierarchical structures and result in the strong adsorption capacity. This allows more efficient transport for the reactant molecules to the active sites, hence enhancing the efficiency of photocatalysis. Second, the high surface-to-volume ratios of nanosheets are in favor of the transfer of electrons and holes and facilitate the degradation of pollution molecules. The prevention of the unwanted aggregation of the nanosheets fixed in the frame of architectures is also helpful in maintaining the high active surface area [26,50]. Compared to **S2**, the slightly higher photocatalytic activity of **S1** can be attributed to its larger BET surface area (Table 1).

4. Conclusions

In summary, two kinds of novel BiOBr hierarchical microspheres have been successfully prepared via a facile, rapid and reliable microwave-assisted solvothermal route. Experiments indicated that both samples exhibited strong adsorption capacities for MO and RhB. The Langmuir adsorption isotherm was applicable to describe the removal processes. The maximum removal capacity of **S1** was found to be 15.3 mg/g for MO. Furthermore, they can also greatly decomposed MO, RhB and phenol under UV irradiation. The higher photocatalytic activities of sample **1** might be ascribed to its novel structures, large BET surface area and strong adsorption capacities. Compared to existing solution-phase synthetic methods using hydrothermal or solvothermal reaction, this work provides a facile, rapid, low-cost pathway to novel BiOBr nanoarchitectures.

Acknowledgments

This work was supported by the National Basic Research Program of China (Nos. 2006CB806104 and 2007CB925102), Natural Science Grant of China (No. 20721002) and the US National Science Foundation.

References

[1] O. Ligrini, E. Oliveros, A. Braun, Chem. Rev. 93 (1993) 671.
[2] M.F. Zhao, Z.B. Tang, P. Liu, J. Hazard. Mater. 158 (2008) 43.
[3] A. Kaur, U. Gupta, J. Mater. Chem. 19 (2009) 8279.
[4] M.F. Zhao, P. Liu, Micropor. Mesopor. Mater. 211 (2008) 419.
[5] D.J. Yang, Z.F. Zheng, H.Y. Zhu, H.W. Liu, X.P. Gao, Adv. Mater. 20 (2008) 2777.
[6] K.V. Baiju, S. Shukla, S. Biju, M.L.P. Reddy, K.G.K. Warrier, Mater. Lett. 63 (2009) 923.
[7] E. Forgacs, T. Cserhati, G. Oros, Environ. Int. 30 (2004) 953.
[8] R.P.M. Fernando, F.S. Samanta, J.M.O. Jose, L.F. Jose, Carbon 41 (2003) 811.
[9] S.K. Parida, S. Dash, S. Patel, B.M. Mishra, Adv. Colloid Interface Sci. 121 (2006) 77.
[10] G. Crini, Prog. Polym. Sci. 30 (2005) 38.
[11] J. Sato, H. Kobayashi, K. Ikarashi, N. Saito, H. Nishiyama, Y. Inoue, J. Phys. Chem. B 108 (2004) 4369.
[12] C.Y. Yan, P.S. Lee, J. Phys. Chem. C 113 (2009) 14135.
[13] J.H. Huang, K.N. Ding, Y.D. Hou, X.C. Wang, X.Z. Fu, ChemSusChem 1 (2008) 1011.
[14] S. Cho, S. Kim, J.W. Jang, S.H. Jung, E. Oh, B.R. Lee, K.H. Lee, J. Phys. Chem. C 113 (2009) 10452.
[15] Y.X. Wang, X.Y. Li, G. Lu, X. Quan, G.H. Chen, J. Phys. Chem. C 112 (2008) 7332.
[16] J.J. Yuan, H.D. Li, S.Y. Gao, Y.H. Lin, H.Y. Li, Chem. Commun. (2010) 3119.
[17] S. Song, J.J. Tu, Z.Q. He, F.Y. Hong, W.P. Liu, J.M. Chen, Appl. Catal. A: Gen. 378 (2010) 169.
[18] Q.Y. Li, T. Kako, J.H. Ye, Appl. Catal. A: Gen. 375 (2010) 85.
[19] Y.Q. Wang, G.Z. Wang, H.Q. Wang, C.H. Liang, W.P. Cai, L.D. Zhang, Chem. Eur. J. 16 (2010) 3497.
[20] H.Y. Xiao, Z.H. Ai, L.Z. Zhang, J. Phys. Chem. C 113 (2009) 16625.
[21] J.S. Hu, L.S. Zhong, W.G. Song, L.J. Wan, Adv. Mater. 20 (2008) 1.
[22] X. Zhang, L.Z. Zhang, T.F. Xie, D.J. Wang, J. Phys. Chem. C 113 (2009) 7371.
[23] Y.Q. Lei, G.H. Wang, S.Y. Song, W.Q. Fan, M. Pang, J.K. Tang, H.J. Zhang, Dalton Trans 39 (2010) 3273.
[24] W.D. Wang, F.Q. Huang, X.P. Lin, J.H. Yang, Catal. Commun. 9 (2008) 8.
[25] M. Shang, W.Z. Wang, L. Zhang, J. Hazard. Mater. 167 (2009) 803.
[26] J. Zhang, F.J. Shi, J. Lin, D.F. Chen, J.M. Gao, Z.X. Huang, X.X. Ding, C.C. Tang, Chem. Mater. 20 (2008) 2937.
[27] X. Zhang, Z.H. Ai, F.L. Jia, L.Z. Zhang, J. Phys. Chem. C 112 (2008) 747.
[28] G.A. Tompsett, W.C. Conner, K.S. Yngvesson, ChemPhysChem 7 (2006) 296.
[29] I. Bilecka, I. Djerdj, M. Niederberger, Chem. Commun. (2008) 886.
[30] J.C. Yu, X.L. Hu, Q. Li, L.Z. Zhang, Chem. Commun. (2005) 2704.
[31] S.H. Kim, S.Y. Lee, G.R. Yi, D.J. Pine, S.M. Yang, J. Am. Chem. Soc. 128 (2006) 10897.
[32] Z. Liu, X.D. Wen, X.L. Wu, Y.J. Gao, H.T. Chen, J. Zhu, P.K. Chu, J. Am. Chem. Soc. 131 (2009) 9405.
[33] Q. Zhang, S.J. Liu, S.H. Yu, J. Mater. Chem. 19 (2009) 191.
[34] G.B. Cai, S.F. Chen, L. Liu, J. Jiang, H.B. Yao, A.W. Xu, S.H. Yu, CrystEngComm 12 (2010) 234.
[35] S.J. Liu, J.Y. Gong, B. Hu, S.H. Yu, Cryst. Growth Des. 9 (2009) 203.
[36] R.L. Penn, J.F. Banfield, Science 281 (1998) 969.
[37] V.M. Yuwono, N.D. Burrows, J.A. Soltis, R.L. Penn, J. Am. Chem. Soc. 132 (2010) 2163.
[38] H. Cölfen, M. Antonietti, Angew. Chem. Int. Ed. 44 (2005) 5576.
[39] S. Wohlrab, N. Pinna, M. Antonietti, H. Cölfen, Chem. Eur. J. 11 (2005) 2903.
[40] A.W. Xu, M. Antonietti, H. Cölfen, Y.P. Fang, Adv. Funct. Mater. 16 (2006) 903.
[41] M. Niederberger, H. Cölfen, Phys. Chem. Chem. Phys. 8 (2006) 3271.
[42] M.S. Mo, S.H. Lim, Y.W. Mai, R.K. Zheng, S.P. Ringer, Adv. Mater. 20 (2008) 339.
[43] X.W. Lu, X.Z. Li, F. Chen, C.Y. Ni, Z.G. Chen, J. Alloy Compd. 476 (2009) 958.
[44] H.X. Zhong, Y.L. Ma, X.F. Cao, X.T. Chen, Z.L. Xue, J. Phys. Chem. C 113 (2009) 3461.
[45] P. Kubelka, F. Munk, Z. Tech. Phys. 12 (1931) 593.
[46] D.G. Barton, M. Shtein, R.D. Wilson, S.L. Soled, E. Iglesa, J. Phys. Chem. B 103 (1999) 630.
[47] J.W. Kramer, S.A. Isaacs, V. Manivannan, J. Mater. Sci. 44 (2009) 3387.
[48] J.M. Herrmann, H. Tahiri, Y. Ait-Ichou, G. Lassaletta, A.R. González-Elipe, A. Fernádez, Appl. Catal. B 13 (1997) 219.
[49] R.G. Chen, J.H. Bi, L. Wu, Z.H. Li, X.Z. Fu, Cryst. Growth Des. 9 (2009) 1775.
[50] J.S. Hu, L.L. Ren, Y.G. Guo, H.P. Liang, A.M. Cao, L.J. Wan, C.L. Bai, Angew. Chem. Int. Ed. 44 (2005) 1269.